

## New insights into the mechanisms of seismicity in the Azle area, North Texas

Rongqiang Chen<sup>1</sup>, Xu Xue<sup>1</sup>, Jaeyoung Park<sup>1</sup>, Akhil Datta-Gupta<sup>1</sup>, and Michael J. King<sup>1</sup>

### ABSTRACT

We have performed a site-specific study of the mechanics of induced seismicity in the Azle area, North Texas, using a coupled 3D fluid flow and poroelastic simulation model, extending from the overburden into the crystalline basement. The distinguishing feature of our study is that we account for the combined impact of water disposal injection and gas and water production on the pore pressure and stress distribution in this area. The model is calibrated using observed injection wellhead pressures and the location, timing, and magnitude of seismic events. We used a stochastic multiobjective optimization approach to obtain estimated ranges of fluid flow and poroelastic parameters, calibrated to the pressure, rate, and seismic event data. Mechanisms for induced seismicity were examined using these calibrated models. The calibrated models indicate no

fluid movement or pressure increase in the crystalline basement, although there is plastic strain accumulation for the weaker elements along the fault in the basement. The accumulation of strain change appears to be caused by the unbalanced loading on different sides of the fault due to the differential in fluid injection and production. Previous studies ignored the produced gas volume, which is almost an order of magnitude larger than the produced water volume under reservoir conditions and which significantly impacts the pore pressure in the sedimentary formations and the stress distribution in the basement. A quantitative analysis indicates that the poroelastic stress changes dominate in the basement with no noticeable change in pore pressure. Even though the low-permeability faults in the basement are not in pressure communication with the Ellenburger formation, the poroelastic stresses transmitted to the basement can trigger seismicity without elevated pore pressure.

### INTRODUCTION

The number of seismic events in the Fort Worth Basin has been increasing since 2007. Near the Azle area, a cluster of seismic events was recorded from late 2013 to early 2014, including two widely felt  $M_w$ 3.6 events. No significant earthquake had been felt prior to 2007 based on more than 40 years of seismic monitoring (Frohlich et al., 2011, 2016). There have been several studies to investigate the cause of the more recent seismic events, and many of them conclude that the injection of wastewater into the subsurface near faults and reactivation of the faults are the primary contributing factors (Frohlich et al., 2011, 2016; Gono et al., 2015; Hornbach et al., 2015; Schwab et al., 2017). Gono et al. (2015) investigate the relationship between disposal water injection and seismic events in the Fort Worth Basin. Using single-phase fluid flow simulation and historical earthquake data, they find that there is a

spatial and temporal correlation between pore pressure increase and seismic events. Hornbach et al. (2015) consider several factors that could lead to seismic events near Azle such as lake-level variations, natural tectonic stress, and stress changes associated with oil and gas production activities. Hornbach et al. (2015) construct single-phase flow models for the Ellenburger formation, a shallowly dipping dolomitic limestone that overlies the crystalline basement and has been used for disposal of large volumes of saline oilfield wastewater (Sullivan et al., 2006; Pollastro et al., 2007). They observe that with different parameter combinations, excess pore pressure at the fault could range from 0.01 to 0.14 MPa. The predicted pore pressure increases at the fault are found to be sufficient to trigger earthquakes when faults are critically stressed (Reasenber and Simpson, 1992; Stein, 1999).

Previous studies at Azle did not solve the coupled fluid flow and geomechanical (poroelastic stress) equations to explicitly model the

Manuscript received by the Editor 15 May 2018; revised manuscript received 4 September 2019; published ahead of production 16 October 2019; published online 22 November 2019.

<sup>1</sup>Texas A&M University, Harold Vance Department of Petroleum Engineering, College Station, Texas, USA. E-mail: jerry397@tamu.edu; xu.xue@tamu.edu; pjy7026@tamu.edu; datta-gupta@tamu.edu (corresponding author); mike.king@tamu.edu.

© 2019 Society of Exploration Geophysicists. All rights reserved.

plastic deformation and the resulting implications for fault activation and induced seismicity, although there have been previous efforts to include geomechanical effects to analyze the potential linkage between fluid injection and seismic events. Fan et al. (2016) investigate an  $M_w$ 4.8 earthquake near Timpson, East Texas, relating the event to geomechanical response of the adjacent fault after nearby wastewater injection. They conduct coupled fluid flow and poroelastic simulations to compute stress and pore pressure along the fault associated with the wastewater injection. Based on the Mohr-Coulomb failure criteria, they assess fault slip with the estimated in situ stress magnitude and direction, fault strike and dip, and permeability of the layer where fluid was injected. Chang and Yoon (2018) perform 3D fully coupled poroelastic modeling of induced seismicity along multiple faults to predict magnitude, rate, and location of potential seismic events. They conclude that the use of 3D coupled poroelastic modeling helps reduce the uncertainty in seismic hazard prediction by considering hydraulic and mechanical interaction between faults and bounding formations. Zhai and Shirzaei (2018) use a basin-wide fluid flow and geomechanical model to investigate seismic hazards in the Barnett Shale, Texas. They relate the Coulomb failure stress change to the seismicity rate and use it as a representation of seismic hazard. They conclude that the contribution of poroelastic stresses to Coulomb failure stress change is approximately 10% of that of pore pressure. However, the model was not calibrated with historical pressure data and the stress change from gas production was not considered. The physical mechanisms behind induced seismicity on faults have also been investigated and discussed in several previous studies (Segall, 1989; Segall et al., 1994; Ellsworth, 2013; Segall and Lu, 2015; Chang and Segall, 2016a, 2016b).

In this study, we focus on the seismicity in the Azle area in North Texas, which experienced a series of seismic events from November

2013 through April 2014. We use coupled fluid flow and geomechanical simulation to numerically solve for the 3D stress/strain field and the pore pressure distribution. For the first time, we account for the reservoir withdrawal created by the gas production. We also calibrate the simulation model to observed injection well pressure data as well as the magnitude and timing of the seismic events to constrain the range of uncertain fluid flow and poroelastic parameters. We use a stochastic multiobjective model calibration that yields an ensemble of models that are consistent with the historical data. All of these models seem to indicate that unbalanced loading on different sides of the critically stressed fault in the crystalline basement resulted in accumulation of plastic strain change, leading to stress changes capable of causing the observed earthquakes in the area.

## METHODOLOGY

### Overall workflow

We focus on the seismicity in the Azle area in North Texas. The events occurred along two northeast-striking, steeply dipping conjugate faults. To assess the potential linkage between the seismic events and the nearby oil and gas field operations, we built a 3D coupled fluid flow and geomechanical model consisting of the overburden, the Marble Falls, the Barnett, the Ellenburger, and the crystalline basement. In the simulation model, we include two injection wells in the Ellenburger and 70 production wells in the Barnett, a shale gas producing formation. A stochastic multiobjective optimization is used to generate an ensemble of models calibrated with injection well pressure data and seismic events (see Appendix A for details). The calibrated models are then used to analyze the mechanisms of induced seismicity at the Azle site. The overall workflow is illustrated in Figure 1.

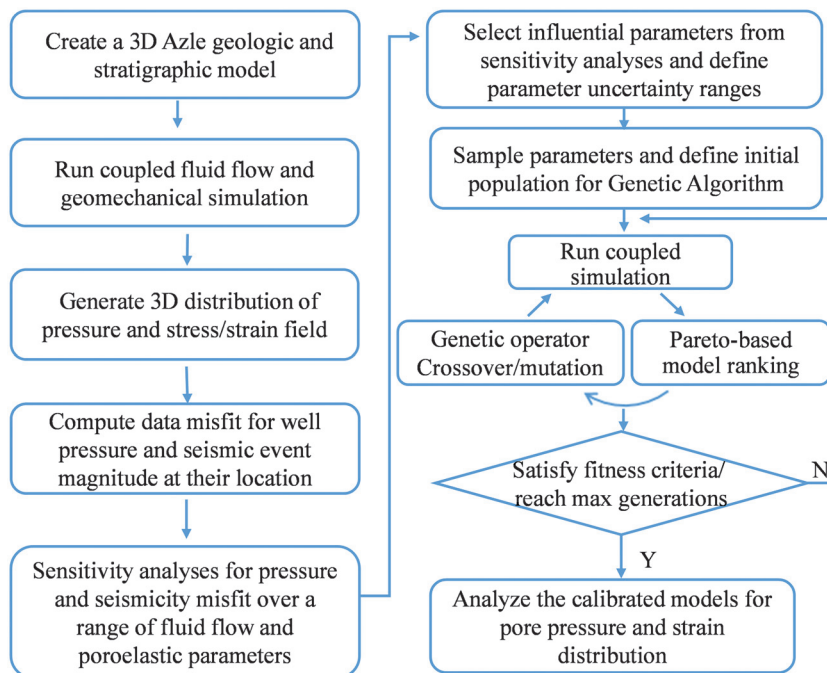


Figure 1. Workflow for the Azle seismicity study using coupled flow and geomechanical modeling.

### Model data sources

To understand the mechanism of seismicity in the Azle area, our study integrates a wide range of data to build and calibrate the 3D coupled fluid flow and geomechanical model. The geologic model is built following the previous studies (Hornbach et al., 2015; Hennings et al., 2016). The faults were constructed using fault interpretations of Hornbach et al. (2015) and the public records from the Railroad Commission of Texas (Railroad Commission of Texas, 2015a, 2015b). The dynamic injection data of rate and pressure of the two saltwater disposal (SWD) disposal wells are available through the H-10 form in the Railroad Commission of Texas website (Railroad Commission of Texas, 2018a). As in the previous study by Hornbach et al. (2015), our study includes only two SWD disposal wells. This is justified because an estimate of the average pressure change in the Azle area due to the two local injectors is found to be almost an order of magnitude higher than the basin-scale average pressure change from all of the injectors based on a flowing material balance calculation (Dake, 1983; Hornbach et al., 2016).

The dynamic production data consist of gas and water production from 70 producing wells. The gas production data are available on the Railroad Commission of Texas website (Railroad Commission of Texas, 2018b). The water production data are obtained from the “DrillingInfo” database (Drillinginfo, 2018). Seismic event data including the event time, magnitude, hypocenter location, and the location uncertainty are obtained from Southern Methodist University (SMU) catalogs (Hornbach et al., 2015; DeShon et al., 2018).

### Geologic model: Background

The Azle geologic and fault model used in this study follows the previous study by Hornbach et al. (2015) with additional details from the Texas Bureau of Economic Geology (Henning et al., 2016). We have extended the geologic model to include the overburden and the crystalline basement where most of the earthquakes have occurred. The structural model consists of two steeply dipping conjugate faults around which most of the earthquakes were recorded.

Faults in the region were constrained by an integrating analysis of stratigraphic mapping, structural interpretation, earthquake hypocenters (Hornbach et al., 2015), and review of public records from the Railroad Commission of Texas (2015a, 2015b). Our model includes two northeast-striking normal faults in the model: Azle and Azle Antithetic. These faults are part of the Llano Fault System in the Fort Worth Basin as described by Ewing (1991). The lateral extent, strike, and general dip of the faults were constrained by 3D interpretation and earthquake hypocenter location.

The Newark East Gas Field (NEGF) is the major gas-producing field in the Fort Worth Basin. Hydraulic fracturing is routinely applied to produce gas from the low-permeability Barnett Shale. Some hydraulically fractured wells can unintentionally produce significant volumes of water from the underlying high-permeability Ellenburger formation (Hornbach et al., 2016). Produced water is reinjected through disposal wells completed in the Ellenburger formation. Low-permeability Precambrian granite basement underlies the Ellenburger formation, and most of the Azle earthquake events have occurred in this unit. The seismic events ( $M_w \geq 2$ ) are shown in Figure 2. Out of 32 seismic events, 25 events are adjacent to the faults, lying within the hypocenter uncertainty range provided by the SMU seismic catalog (Hornbach et al., 2015; DeShon et al., 2018). Additional seismic stations deployed by SMU were intended to reduce the location uncertainty after the early 27 earthquakes near the Azle were reported by the United States Geological Survey (USGS). A schematic of the 3D geologic model is shown in Figure 2. In this layer-cake Azle model, the fluid flow and poroelastic properties are considered uniform within each zone except at the fault cells.

Table 1 shows the fluid flow and poroelastic properties for each zone used in the base case model along with their corresponding sources. Figure 3 shows the Mohr circle showing the stress state (Lund Snee and Zoback, 2016) and the Mohr-Coulomb failure envelope of the fault for the base case at a depth of 3048 m, which is the top of the basement. As noted by Lund Snee and Zoback (2016) and Quinones et al. (2018), the fault is nearly critically stressed.

### Forward simulation model

A coupled fluid flow and geomechanical simulation model is used to compute the evolution of the 3D pressure and stress/strain

fields in the Azle area during the period of fluid injection and production. The Azle simulation model consists of uniform grid cells ( $160 \times 160$  m) areally, and varying cell dimensions vertically, with higher resolution in the Barnett and Ellenburger formations. The model has 1 layer for the overburden and 1 layer for the Marble Falls to provide geomechanical loading to the reservoir; 5 layers for the Barnett, which is the producing zone; 5 layers for the Ellenburger, which is the injection zone; and 10 layers for the crystalline basement where most of the earthquake events occurred. The overburden has the lowest vertical resolution of 2000 m, and the Barnett has the highest vertical resolution of 23 m. There are two tilted faults intersecting just below the Ellenburger, and the major fault extends down to the bottom of the basement (Figure 2). The fault cells have distinct fluid flow and poroelastic properties from the adjacent formations (Table 1). The base case simulation model consists of 70 producers completed in the Barnett and two SWD disposal wells completed in the Ellenburger (Figure 4) with a total simulation study period of 12 years (supplementary information can be accessed through the following link: S1). Hydraulic fractures create high-permeability regions near the producers, so the permeability near the producers is enhanced to honor the historical production rates at the wells. The injected wastewater volume and gas production data are available in the Railroad Commission of Texas website (Railroad Commission of Texas, 2018b). The water production data are from the DrillingInfo database (Drillinginfo, 2018). The water production data were cross-checked with the data provided by the operator (XTO Energy Inc.) for selected wells to ensure accuracy.

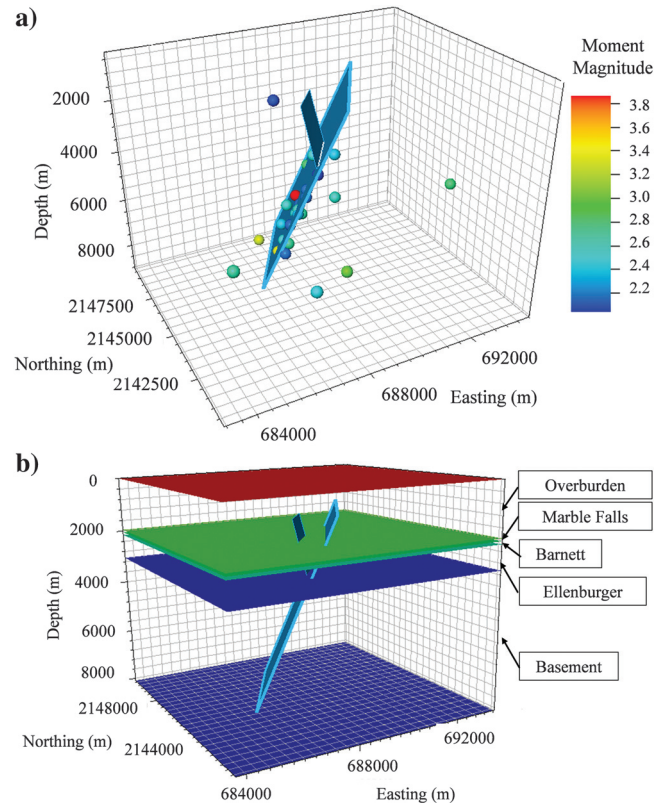


Figure 2. (a) Azle area fault location and the locations of the earthquake events ( $M_w \geq 2$ ). (b) A schematic of the Azle geologic model.

Our forward model uses coupled fluid flow and poroelastic simulation to numerically solve the continuity and the momentum balance equations in a sequential manner. The continuity equation solves for the formation pore pressure and is given by

$$\frac{d}{dt} [\phi \rho_f (1 - \varepsilon_v)] - \nabla \cdot \left[ \rho_f \frac{k}{\mu_f} (\nabla p - \rho_f g \nabla D) \right] = Q_f, \quad (1)$$

where  $\phi$  is the porosity,  $\rho_f$  is the density of fluid,  $\varepsilon_v$  is the volumetric strain,  $k$  is the permeability,  $\mu_f$  is the fluid viscosity,  $g$  is the gravitational constant,  $D$  is the depth from a reference pressure data, and  $Q_f$  is the mass source term.

The momentum balance equation solves for formation displacement and can be expressed as

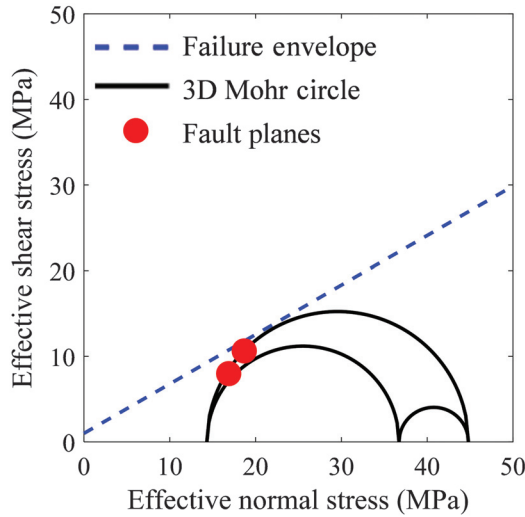


Figure 3. Initial stress state and the Mohr-Coulomb failure envelope for the base case Azle model.

$$\nabla[\mathbf{C} : \frac{1}{2}(\nabla \mathbf{u} + (\nabla \mathbf{u})^T)] = -\nabla[\alpha p] \mathbf{I} + \mathbf{B}, \quad (2)$$

where  $\mathbf{C}$  is the tangential stiffness tensor,  $\mathbf{u}$  is the displacement,  $\alpha$  is the Boit's number,  $p$  is the pressure,  $\mathbf{I}$  is the identity matrix, and  $\mathbf{B}$  is the body force.

The momentum balance equation is solved using a finite-element scheme, whereas the continuity equation is solved using a finite-difference scheme. The two solutions are sequentially coupled (Computer Modeling Group, 2016). We obtain the 3D stress/strain and pressure distribution for the entire simulation domain at each simulation time step.

The forward simulation model is calibrated to match the observed wellhead pressure data and the magnitude and timing of the seismic

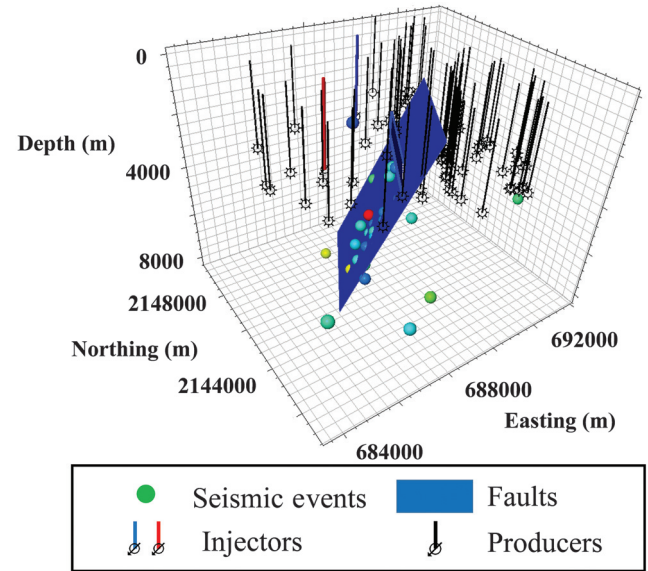


Figure 4. Injection/production well locations and seismic event locations with respect to the Azle faults.

**Table 1. Fluid flow and poroelastic properties for the Azle base case simulation model.**

	Overburden	Marble Falls	Barnett	Ellenburger	Basement	Fault	Reference
Permeability (mD)	190	0.01	1.00E-05	30	1.00E-04	1.00E-03	Hornbach et al. (2015)
Porosity	0.2	0.2	0.06	0.055	0.05	Same as formation	
Pore pressure			23,082 kPa @ 2046 m				Railroad Commission of Texas (2015b)
Effective vertical stress gradient			14.7 kPa/m				Simpson, (1997) and Lund Snee and Zoback (2016)
Effective minimum horizontal stress gradient			4.5 kPa/m				
Anderson fault parameter, $A_\phi$			0.74				
Direction of horizontal stress			N28.8E				
Young's modulus (kPa)	1.44E+07	6.00E+07	4.00E+07	6.00E+07	4.30E+07	4.00E+07	Wang (2000), Tutuncu (2010), Rutqvist et al. (2013), and Sone and Zoback (2013)
Poisson's ratio	0.2	0.2	0.23	0.2	0.27	0.25	
Cohesion (kPa)	2.00E+04	2.00E+04	2.00E+04	2.00E+04	2.00E+04	1.00E+03	
Friction angle (°)	30	30	30	30	30	30	

events to reduce the range of the uncertain parameters. The simulated well bottom hole pressure (BHP) can be directly obtained from flow simulation and compared with the calculated BHP obtained from the measured wellhead pressure. This requires converting the wellhead pressure data to the bottom hole conditions, a routine calculation in petroleum reservoir engineering (Govier and Aziz, 1972; Beggs and Brill, 1973; Chen, 1979; Taitel et al., 1982; Bradley, 1987; Ansari et al., 1990; Economides et al., 2013). The details of this calculation are given in Appendix B.

The poroelastic simulation calculation checks the failure status for each cell in the 3D model at every time step and accumulates the plastic strain after the rock failure. The plastic strain/deformation is the strain after a cell reaches Mohr-Coulomb failure and is calculated using the generalized plasticity model based on the Mohr-Coulomb yield surface (Vermeer and De Borst, 1984; Computer Modeling Group, 2016). All of the accumulated plastic strains are then used to calculate the seismic moment magnitude (Sanz et al., 2015; Castiñeira et al., 2016; Lele et al., 2016; Park et al., 2016). The computed seismic moment magnitude is compared with the observed seismic event magnitudes during model calibration. The seismic moment tensor is used to model the seismicity induced by fault activation. The seismic moment tensor is represented by the following equation (Aki and Richards, 2002):

$$M_{pq} = \int_V c_{pqrs} \Delta e_{rs} dV, \quad (3)$$

where the repeated indices indicate summation. Here,  $c_{pqrs}$  is the stiffness tensor or the elastic modulus tensor consisting of Young's modulus and Poisson's ratio. Note that during model calibration, we adjust Young's modulus and Poisson's ratio. Thus, the elastic tensor dynamically evolves. The term  $\Delta e_{rs}$  is the change in plastic strain by deformation, which is accumulated after a cell reaches the Mohr-Coulomb failure criteria. The  $L_2$  norm of the seismic moment tensor is used to obtain the intensity of the seismic moment ( $M_0$ ) (Dahm and Krüger, 2014):

$$M_0 = \|M_{pq}\|_{L_2}. \quad (4)$$

The seismic moment magnitude is calculated as follows (Kanamori, 1977):

$$M_w = \frac{\log M_0 - 16.1}{1.5} + 4.667. \quad (5)$$

The observed wellhead pressure and seismic data are matched by adjusting the fluid flow and poroelastic properties using a multiobjective stochastic optimization method. Details of the model calibration are discussed in the next section and in Appendix A.

A distinctive feature in the current model compared with previous studies is the inclusion of gas production. Previous studies incorporated the pressure reduction due to brine production from the Ellenburger formation. However, hydrocarbon gas production can contribute to greater reservoir depletion compared to brine production. The brine is produced from the Ellenburger formation because the hydraulic fractures propagate through the Barnett into the Ellenburger formation (Hornbach et al., 2015). Especially in regions where the Viola Shale is absent below the Barnett Shale, as in the Azle area (Pollastro et al., 2007; Loucks et al., 2009), the producers in the Barnett are in direct pressure communication with the

Ellenburger formation. Our results show that ignoring gas production leads to significant underestimation of the reservoir fluid withdrawal and reservoir pressure depletion. We convert the surface gas production to bottom hole conditions and use the equivalent reservoir fluid withdrawal rates. Details are presented in Appendix C. Because the pore pressure is primarily impacted by the total reservoir fluid withdrawal of all phases, the equivalent reservoir fluid withdrawal rates help ensure that the material balance is preserved in reservoir conditions for single-phase and multiphase flow simulations. Figure 5 shows the water production, gas production, and the total fluid withdrawal under reservoir conditions. Note that the reservoir volume of the produced gas is almost one order of magnitude larger than the produced water volume.

It is worth pointing out that the coupled simulation model used here only requires specification of the total fluid withdrawal rate, whereas the individual layer allocations are computed based on the layer productivity indices (Computer Modeling Group, 2016).

### Model calibration using multiobjective optimization

In this study, we minimize two objective functions for model calibration: injector BHP misfit and seismic moment magnitude misfit at their respective locations and times.

The injector BHP misfit is calculated using the following equation:

$$\text{obj}_{\text{BHP}} = \log \left( \sum_{j=1}^{N_{\text{well}}} \sqrt{\sum_{i=1}^{N_{\text{time}}} (\text{BHP}_{i,j}^{\text{obs}} - \text{BHP}_{i,j}^{\text{cal}})^2} \right), \quad (6)$$

where  $N_{\text{well}}$  is the total number of history matching wells,  $N_{\text{time}}$  is the total number of data points for each well, superscript obs indicates the observed data, and superscript cal indicates the calculated value from the simulation.

Figure 6 illustrates the seismic moment magnitude misfit calculation. It is the difference between the seismic moment magnitude based on the plastic strain after rock failure and the observed seismic event magnitude at the time and location of the observed seismic event. It is given by

$$\text{obj}_{\text{magnitude}} = \sqrt{\sum_{i=1}^{N_{\text{event}}} (M_w^{\text{obs}} - M_w^{\text{cal}})^2}, \quad (7)$$

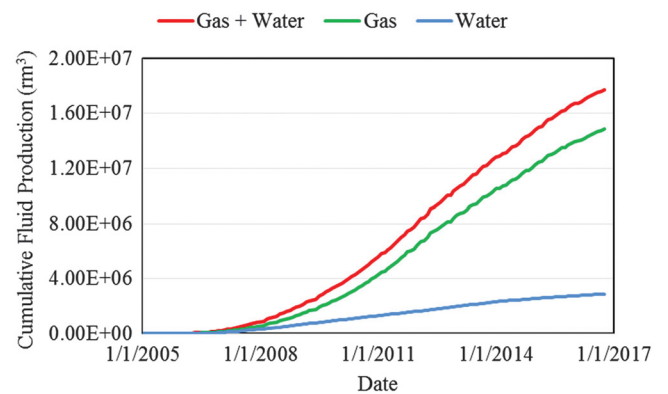


Figure 5. Produced fluid volumes used in this study (at reservoir conditions).

where  $N_{\text{event}}$  is the total number of seismic events being matched,  $Mw_i^{\text{obs}}$  is the observed seismic moment magnitude of event  $i$ , and  $Mw_i^{\text{cal}}$  is the calculated seismic moment magnitude from the simulation within a search radius of seismic event  $i$ . Here, the search radius is given by the average earthquake epicenter uncertainty in the SMU catalog (Hornbach et al., 2015; DeShon et al., 2018). For the events reported in the SMU catalog, the mean epicenter major axes' length is  $570 \pm 362$  m, minor axes' length is  $310 \pm 228$  m, and the depth uncertainty is  $346 \pm 171$  m. At each simulation time step, we check every grid cell within the search radius of each observed seismic event to determine whether it meets the Mohr-Coulomb failure criteria. Once a cell fails, plastic strain accumulation starts for this cell. The cell with the minimum misfit within the search radius of each observed seismic event is used for the objective function calculation. We assume that all of the plastic strain within the cell may release seismically as one single event, which may not always be the case (Bourouis and Bernard, 2007; Guglielmi et al., 2015; McGarr and Barbour, 2017). We use this approach because there are no specific data available for the Azle area to distinguish between seismic and aseismic deformation.

To calibrate the forward model using available injector pressure and seismic moment data, we use a Pareto-based stochastic multi-objective history matching algorithm. Instead of aggregating different misfit functions, the Pareto-based approach ranks the models based on the concept of dominance (see Appendix A). For a minimization problem involving  $n$  objectives defined by objective functions  $f_n$ , solution  $a$  dominates solution  $b$  if all objectives represented by  $a$  are not greater than those of  $b$ , and at least one objective of  $a$  is strictly smaller than the corresponding objective

of  $b$ . The genetic algorithm (GA) (Goldberg, 1989) is used for updating the uncertain parameters during calibration. GA is one of the evolutionary methods for solving optimization problems. It imitates biological principles of evolution: natural selection and survival of the fittest. The evolution starts from a population of randomly generated models with uncertain parameters sampled from a prespecified uniform distribution defined by their respective minimum and maximum values. In each generation, the fitness of every model (the model rank in our study) in the population is evaluated. Multiple models are stochastically selected from the current population (based on their fitness) and modified (recombined and possibly randomly mutated) to form a new population. The new population is then used in the next iteration of the algorithm. Commonly, the algorithm terminates when either the maximum number of generations is reached or a satisfactory fitness level is attained (Yin et al., 2011). Thus, multiple plausible parameter combinations are generated with low-rank populations that match the historical data within a specified tolerance.

## RESULTS: PARAMETER SENSITIVITY ANALYSIS AND HISTORY MATCHING

### Parameter sensitivity analysis

The sensitivity analysis involves forward simulations by changing one parameter at a time to identify the key parameters affecting the objective functions for BHP and seismic moment magnitude (Yin et al., 2011). The parameters with a strong influence on the objective functions are kept for model calibration, and the less-sensitive parameters are discarded.

Figure 7 shows a “tornado plot” illustrating the sensitivity of injector BHP misfit to various parameters. As expected, reservoir fluid flow parameters such as permeability and permeability anisotropy (vertical/horizontal) are the most influential parameters on the list. The BHP misfit is also impacted by the Ellenburger poroelastic properties such as Young's modulus and Poisson's ratio because of their effects on the Ellenburger formation compressibility. The importance of the vertical permeability indicates the impact of pressure communication between the disposal and production intervals. The permeabilities of the Barnett Shale and the crystalline basement are very low for the base case. Thus, the injector BHP is not significantly impacted by their permeability, porosity, and poroelastic properties. From this sensitivity analysis, permeability anisotropy, Ellenburger permeability, Young's modulus, and Poisson's ratio are identified as the primary tuning parameters for BHP calibration.

Figure 8 shows a tornado plot illustrating the sensitivity of the misfit between the simulated seismic moment magnitude and the observed earthquake magnitude. The minimum effective horizontal stress and fault cohesion are the most sensitive parameters here because these determine how close the faults are to a critically stressed state based on the Mohr-Coulomb criteria. The fault Poisson's ratio is important because it is used to construct the stiffness matrix for the moment tensor calculations. The basement permeability is in the nanodarcy range, and there is very little pressure communication from above. Hence, the seismic moment magnitude misfit is mostly affected by its poroelastic parameters. The pressure and seismic moment magnitude misfits show very little sensitivity to the fault permeability.

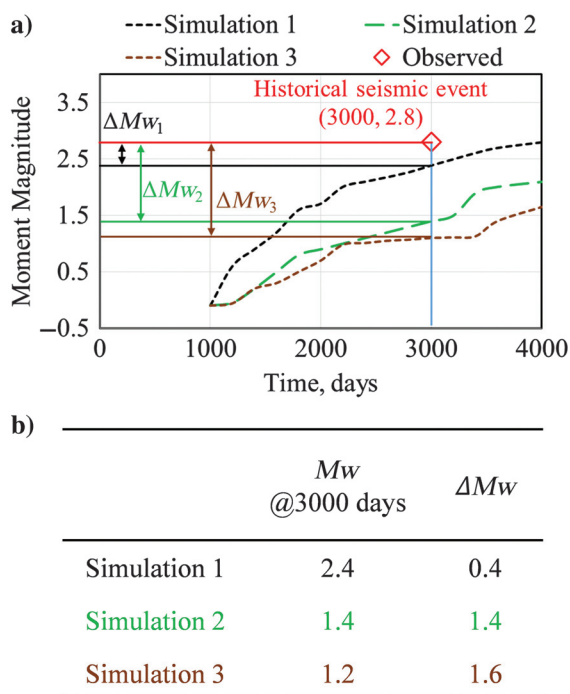


Figure 6. Illustration of the seismic moment magnitude misfit calculation. (a) seismic moment magnitude evolution and (b) seismic moment magnitude misfit calculation.

### Multiobjective history matching and parameter uncertainty

Table 2 shows the poroelastic and fluid flow parameters with a strong influence on objective functions based on the sensitivity analysis and their corresponding ranges. These parameters will be calibrated to match the observed injector BHP and the seismic moment magnitude. Most poroelastic properties have relatively high uncertainty ranges because of limited data or prior knowledge. This makes the model calibration imperative for reducing the parameter ranges. Figure 9a shows the results of the multiobjective history matching using the GA. As expected, the generation 1 population members are scattered to explore the parameter space, whereas the generation 5 population members move toward the bottom left, indicating misfit reduction for BHP and seismic moment magnitude. We also see the formation of a “Pareto front” between BHP and seismic magnitude misfits with multiple generations displaying the trade-off between the misfit functions. Figure 9b shows the quality of seismic moment magnitude match; the rank 1 matches moves toward the unit slope line although with some degree of scatter. However, several of the rank 1 matches show lower calculated seismic moment magnitude compared to the observed seismic magnitude especially for the ( $M_w \geq 3$ ) seismic events. This is consistent with the previous findings that the faults are initially in a critically stressed state and already in a state of plasticity (Zoback et al., 2012; Hornbach et al., 2015; Lund Snee and Zoback, 2016; Quinones et al., 2018; Zhai and Shirzaei, 2018). We did not account for any initial strain accumulation in the faults, and this might introduce biases in the model calibration. However, the methodology of multiobjective optimization allows us to explore what information may be discerned from the data, despite these shortcomings. Furthermore, the use of coupled fluid flow and geomechanical calculation, including Mohr-Coulomb failure, allows us to explore these coupled mechanisms. Figure 9c and 9d shows the BHP history matching result for injectors 1 and 2, respectively. All of the rank 1 models show good agreement with historical pressure data and a decreasing pressure trend over the injection period. The intent of the model calibration is to be as quantitative as possible, and the ensemble-based approach provides error bounds in the parameter estimates. However, the goal here is not to match the observed pressure data exactly given the uncertainty in the field data. Instead, the calibration results in an ensemble of models that match the seismic and pressure data adequately.

Figure 10 shows the parameter ranges before and after history matching. The Ellenburger permeability (2 PERME), fault cohesion (3 COHEF), and fault Poisson’s ratio (8 POISSF) show a significant reduction in range after history

matching. We also observe a reduction in uncertainty range for several other poroelastic parameters. It is important to note that fault cohesion (3 COHEF) and minimum horizontal stress (9 Shmin) move toward lower values, again suggesting that the fault is initially in a critically stressed state (Zoback et al., 2012; Hornbach et al., 2015; Lund Snee and Zoback, 2016; Quinones et al., 2018; Zhai and Shirzaei, 2018). A critically stressed fault can also explain why the matches in Figure 9b show a lower simulated seismic moment magnitude compared to the observed seismic event magnitude. If sufficient quantitative data were available to account for the initial plasticity of the fault elements, the matches to the

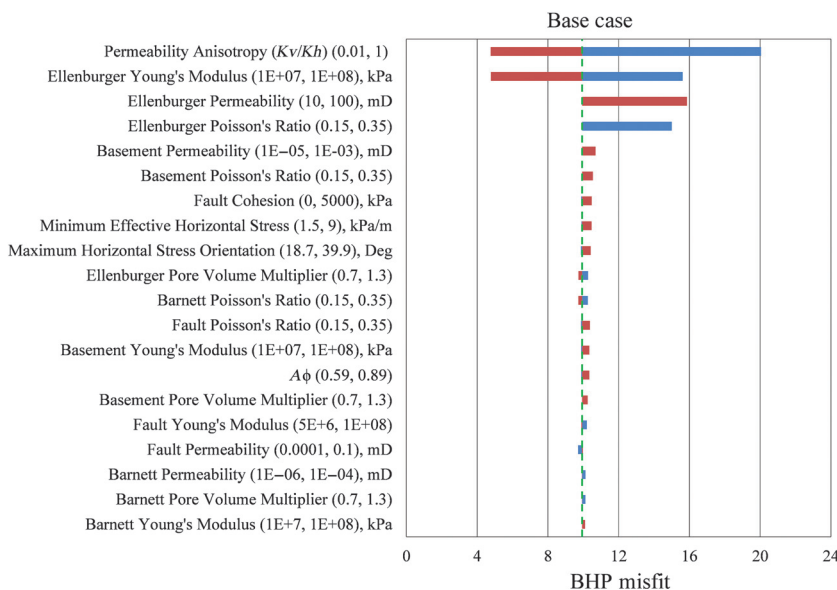


Figure 7. Tornado plot for sensitivity of injector BHP misfit to various fluid flow and poroelastic parameters and their ranges (in parentheses).

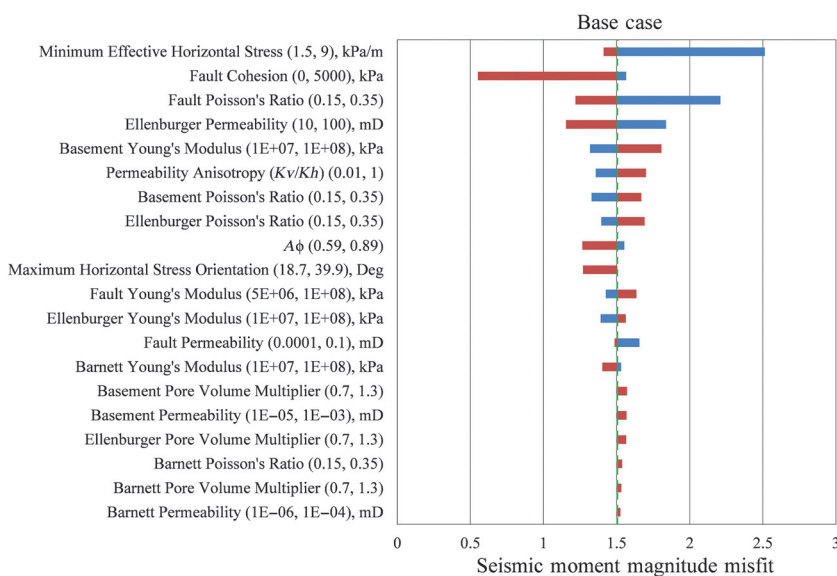


Figure 8. Tornado plot for sensitivity of the seismic moment magnitude misfit to various fluid flow and poroelastic parameters and their ranges (in parentheses).

observed seismic events most likely would have improved in Figure 9b.

Classification tree analysis is used to evaluate the relative parameter importance (Mishra and Datta-Gupta, 2017). The matched models are split into four groups or clusters based on the misfit function quartiles. Cluster 1 has the lowest misfit, and cluster 4 has the highest misfit value. This means that solutions falling into cluster 1 most closely reproduce the observed history, whereas solutions falling into cluster 4 significantly deviate from the history.

Figure 11 shows the binary classification tree for the seismic moment magnitude misfit and the injector BHP misfit. The binary classification tree is generated by recursively finding the variable splits that best separate the output into groups in which a single category dominates (Breiman et al., 1984). The algorithm searches through the variables one by one to find the optimal split within each

variable, and the splits are compared among all of the variables to find the best split for that fork. The process is repeated until all groups contain a single category. Thus, the more dominant variables are generally the splits closer to the tree root. In this study, the minimum horizontal stress (Shmin) and fault Poisson's ratio (POISSF) dominate the seismic moment magnitude misfit. The BHP misfit is most heavily impacted by the Ellenburger permeability (PERME).

It is important to note that if the effective minimum horizontal stress is higher than a threshold value (4.53 kPa/m), all simulation results will significantly deviate from the seismic event history because of the insufficient accumulation of seismic moment magnitude. The minimum horizontal stress gradient is readily obtained from minifrac tests and plays a critical role in evaluating the potential for induced seismicity.

## RESULTS AND DISCUSSION

Wastewater disposal has been associated with induced seismicity, and much of the literature has focused on reservoir pore pressure increase after injection as the primary mechanism for the seismicity (Zhang et al., 2013; Gono et al., 2015; Hornbach et al., 2015; Fan et al., 2016; Zhai and Shirzaei, 2018). However, our results indicate that pore pressure increase is not present in the Azle basement fault and may not be the primary reason for the seismic events at Azle. Previous studies have suggested that the Barnett and Ellenburger formations are not isolated and so will experience pressure communication between the injection and production intervals (Pollastro et al., 2007; Loucks et al., 2009; Hornbach et al., 2015). Our wellhead pressure calibration study reinforces this conclusion. However, when we account for fluid injection and extraction, including the reservoir withdrawal from gas production, we see differential pressure increase and decrease within the Ellenburger on opposite sides of the Azle fault. However, we see no increase in pore pressure in the Azle fault within the basement.

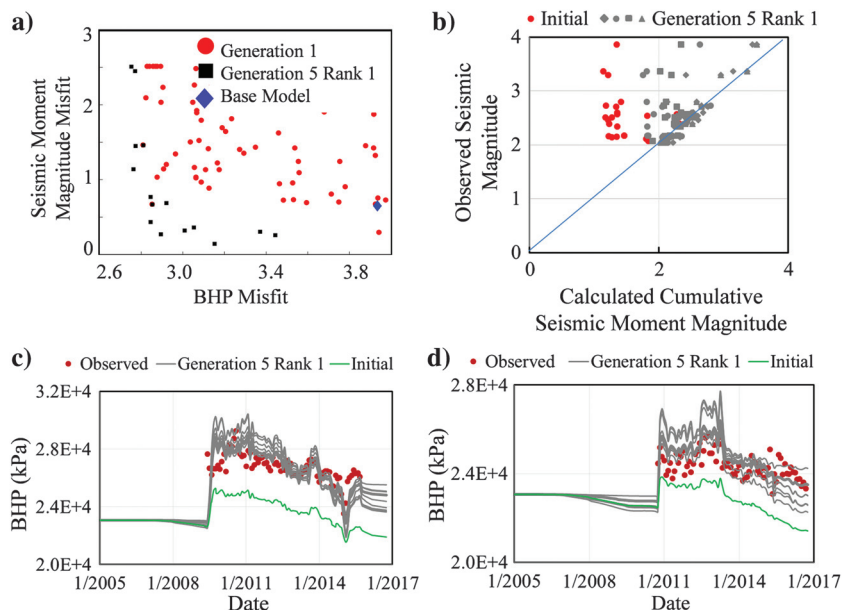


Figure 9. Multiobjective history-matching results. (a) Trade-off between seismic moment magnitude and BHP misfit. (b) Seismic moment magnitude match: initial versus generation 5 rank 1. (c) Injector 1 BHP match: initial versus generation 5 rank 1. (d) Injector 2 BHP match: initial versus generation 5 rank 1.

Table 2. History-matching parameters and ranges.

	Description	Parameter	Base	Low	High
Poroelastic properties	Ellenburger Young's modulus (kPa)	YOUNGE	6.00E+07	1.00E+07	1.00E+08
	Basement Young's modulus (kPa)	YOUNGB	4.30E+07	1.00E+07	1.00E+08
	Fault Young's modulus (kPa)	YOUNGF	4.00E+07	1.00E+07	1.00E+08
	Fault cohesion (kPa)	COHEF	1000	0	5000
	Ellenburger Poisson's ratio	POISSE	0.27	0.15	0.35
	Fault Poisson's ratio	POISSF	0.25	0.15	0.35
	Effective minimum horizontal stress	Shmin	4.5	1.5	9
	Fluid flow properties	Ellenburger pore volume multiplier	PVE	1	0.7
Ellenburger permeability multiplier		PERME	1	0.1	10
Permeability anisotropy		$K_v/K_h$	0.1	0.01	0.2

To further examine the impact of gas production on the reservoir pressure, we performed coupled simulation including only water production. Figure 12 compares the injector BHP using the total fluid extraction rate (gas and water) as in this study versus water production rate only as in the previous study (Hornbach et al., 2015). Using only the water production rate, the simulated BHP deviates significantly from the observed pressure history.

The visualization of streamlines (fluid flow paths) from one of the calibrated models is shown in Figure 13a. Clearly, fluid flow occurs mostly in the Barnett and Ellenburger formations and there is no fluid movement into the basement. Thus, there is no pore pressure change within the basement. However, even with the lack of fluid movement in the basement, Figure 13c and 13d shows that there is noticeable plastic strain accumulation for the weaker elements along the fault. For this specific case shown in Figure 13, the fault Young's modulus and Poisson's ratio are  $6.86e+7$  kPa and 0.16, respectively.

Plastic strain change accumulation is caused by unbalanced loading on different sides of the fault as shown in Figure 14. On the northwest side of the main fault, there are two injectors and 20 producers active at various times during the simulation study. The overall net reservoir volume (the cumulative injection volume minus the cumulative production volume) at the end of the simulation history is approximately  $3.5 \times 10^6$  m<sup>3</sup>. On the other side of the fault, there are 50 active producers at various times during the simulation study, but no injectors. The overall net reservoir volume is approximately  $-8.1 \times 10^6$  m<sup>3</sup>. Even though the reservoir is not completely compartmentalized by the fault (Hornbach et al., 2015), the difference in net reservoir volume change on different sides of the fault creates an unbalanced loading on the basement. The unbalanced loading is evident from the pressure contours displayed on the streamlines in Figure 14c. As suggested in previous studies (McGarr et al., 2002; Ellsworth, 2013; National Research Council, 2013), changes in loading conditions on faults due to fluid extraction and/or injection and associated stress changes can result in earthquakes, even with no direct hydrologic connection. This unbalanced loading can accumulate sufficient plastic strain on the weaker elements of the basement, resulting in stress fields capable of causing the observed earthquakes in the area. The mechanism of unbalanced loading is sensitive to the local imbalance of pressure within the Ellenburger across the Azle fault. The pressure imbalance is controlled by local injection and production.

To further validate our observations, we perform a quantitative analysis to examine the relative contributions of pore pressure change and poroelastic stress change on the Coulomb failure stress change ( $\Delta\tau$ ) (Chang and Segall, 2016a):

$$\Delta\tau = \Delta\tau_s + \mu(\Delta p + \Delta\sigma) = \mu\Delta p + (\Delta\tau_s + \mu\Delta\sigma), \quad (8)$$

where  $\Delta\tau_s$  is the change in the shear stress,  $\Delta\sigma$  is the change in normal stress calculated on the fault,  $\Delta p$  is the change in pore pressure, and  $\mu$  is the friction coefficient.

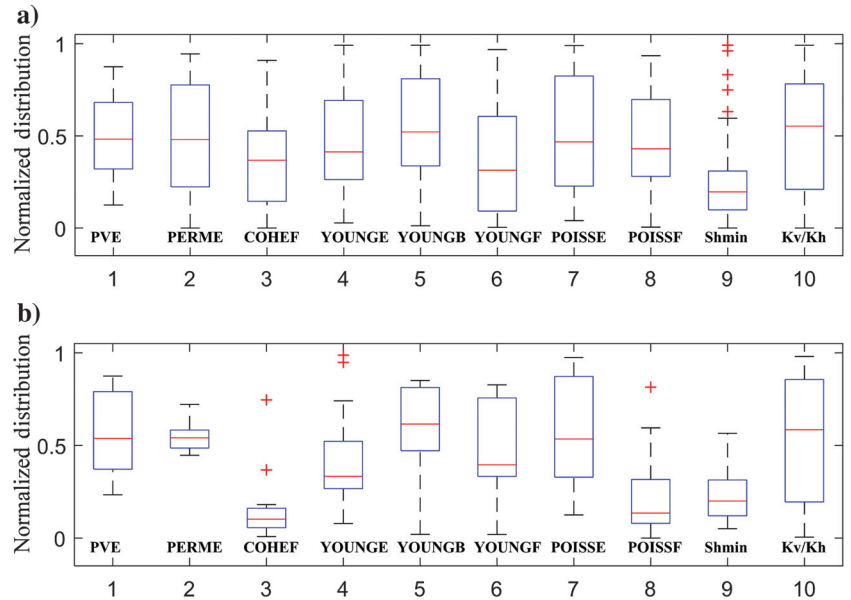


Figure 10. History match parameter ranges: (a) prior distribution and (b) posterior distribution. PVE: Ellenburger pore volume multiplier, PERME: Ellenburger permeability, COHEF: fault cohesion, YOUNGE: Ellenburger Young's modulus, YOUNGB: basement Young's modulus, YOUNGF: fault Young's modulus, POISSE: Ellenburger Poisson's ratio, POISSF: fault Poisson's ratio, Shmin: minimum effective horizontal stress gradient, and  $Kv/Kh$ : vertical permeability over the horizontal permeability anisotropy ratio.

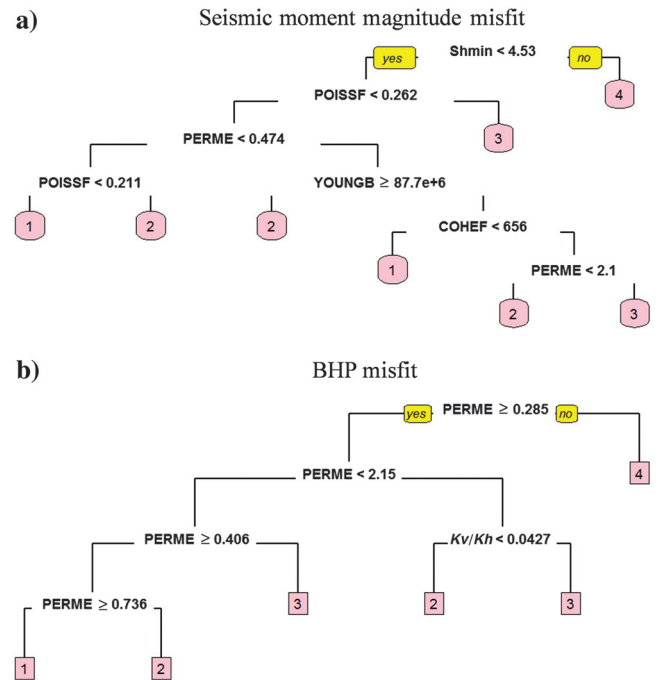


Figure 11. Parameter importance analysis using a classification tree. (a) Seismic moment magnitude misfit and (b) injector pressure misfit. Shmin: minimum effective horizontal stress gradient, POISSF: fault Poisson's ratio, PERME: Ellenburger permeability, YOUNGB: basement Young's modulus, COHEF: fault cohesion, and  $Kv/Kh$ : vertical permeability over horizontal permeability anisotropy ratio. Cluster 1 refers to the best model, and cluster 4 refers to the worst model based on the data misfit. For example, the important parameter ranges for the best-fit models can be understood by following the trail of cluster 1.

Figure 15 shows the change in pore pressure versus the change in poroelastic stress toward the top of the crystalline basement (3.3 km depth). The poroelastic stress changes clearly dominate in the base-

ment with no noticeable change in pore pressure. Even though the low-permeability faults in the basement are not in pressure communication with the Ellenburger formation, the poroelastic stresses

Figure 12. Comparison of injector BHP for the equivalent bottom hole total fluid rate (gas + water) versus water rate only for (a) injector 1 and (b) injector 2.

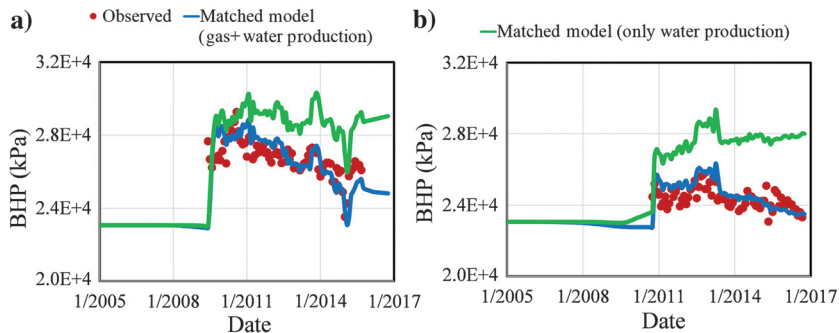


Figure 13. (a) Streamline flow visualization showing no fluid flow within the crystalline basement, (b) seismic event locations, (c) the matched-case plastic strain change JJ component, and (d) the matched-case plastic strain change JK component on 1 January 2014. The blue surface shows the top of the crystalline basement, and the gray surface shows the primary Azle fault.

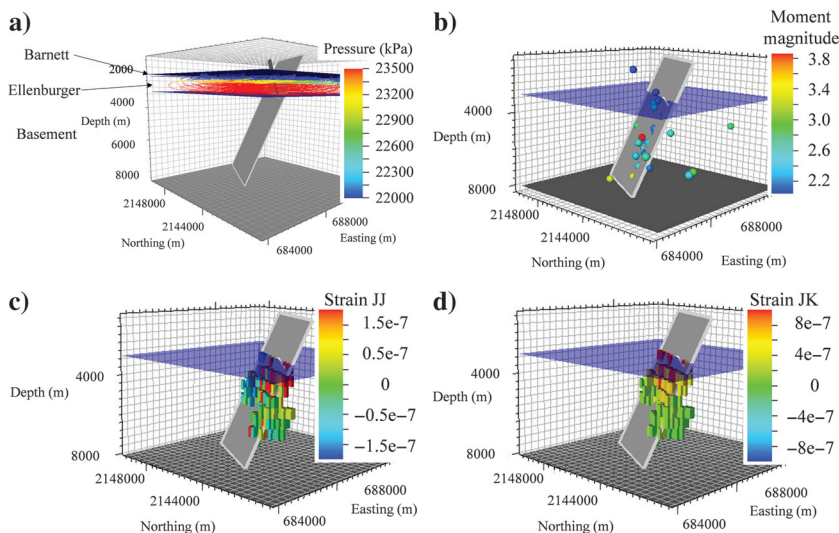
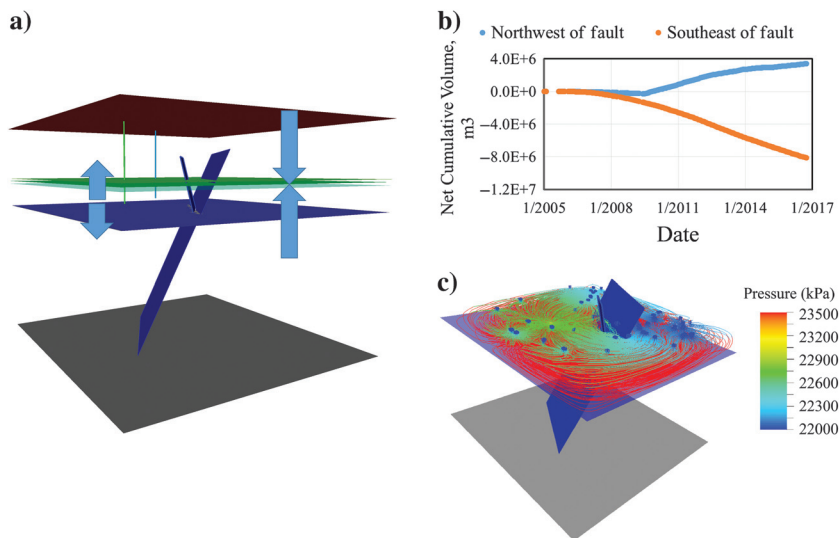


Figure 14. A schematic diagram for the unbalanced loading on different sides of the Azle fault, (b) the difference in net cumulative volume (injection volume - production volume) at different sides of the fault, and (c) streamlined flow visualization showing the pressure imbalance at different sides of the fault.



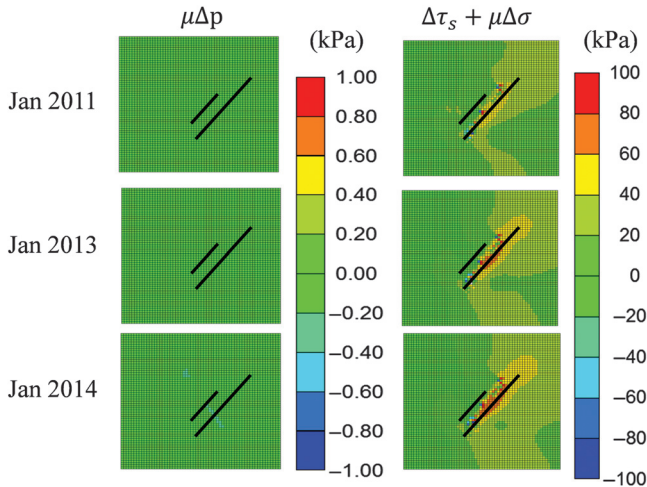


Figure 15. Pore pressure change and poroelastic stress change over time at the top of the crystalline basement (at 3.3 km depth). Note the difference in scales in the figure.

transmitted to the basement can trigger seismicity without elevated pore pressure in the basement fault.

## CONCLUSION

Geomechanical poroelastic interactions have a significant impact on the seismicity observed in the Azle area, North Texas. Unbalanced loading on different sides of the main Azle fault appears to generate an accumulation of plastic strain change in the basement, most likely leading to stresses capable of causing the observed earthquakes in the area. Unlike previous studies, our results indicate that the pore pressure does not increase within the basement fault and that pore pressure increase may not be sufficient to explain the seismicity near the Azle area.

An integrated evaluation of the gas and water production due to hydrocarbon recovery shows that the cumulative gas production is almost an order of magnitude larger than the water production, when corrected to reservoir volumes. The equivalent bottom hole fluid rate (combining reservoir withdrawal from water and gas) used in this study suggests a reduction in Ellenburger pore pressure that is consistent with the observed wellhead pressure trends. We do not see fluid movement or a pressure increase in the crystalline basement, although there is plastic strain accumulation for the weaker elements along the fault in the basement. The accumulation of strain change is caused by unbalanced loading on different sides of the fault. To the northwest of the main fault, there are two injectors and 20 producers, leading to an overall increase in net reservoir volume of approximately  $3.5 \times 10^6 \text{ m}^3$ . To the southeast of the fault, there are 50 producers and an overall net decrease of approximately  $8.1 \times 10^6 \text{ m}^3$ . Although the reservoir is not completely compartmentalized by the fault, this difference in net reservoir volume change on different sides of the fault creates an unbalanced loading to the basement.

A quantitative analysis shows that the poroelastic stress changes dominate in the basement with no noticeable change in pore pressure. Even though the low-permeability faults in the base-

ment are not in pressure communication with the Ellenburger formation, the poroelastic stresses transmitted to the basement can trigger seismicity without elevated pore pressure.

## ACKNOWLEDGMENTS

Authors thank the associate editor and the anonymous reviewers for their constructive comments throughout the peer-review process. This work was supported by Texas A&M University Joint Industry Project, Model Calibration and Efficient Reservoir Imaging (MCERI), and the Texas Seismic Network (TexNet) program at the Bureau of Economic Geology, the University of Texas at Austin. Authors are grateful to Peter Hennings and TexNet research team at BEG for supporting this work and XTO Energy Inc. for providing field data for validation.

## DATA AND MATERIALS AVAILABILITY

Data associated with this research are available and can be obtained by contacting the corresponding author.

## APPENDIX A

### PARETO OPTIMIZATION AND GENETIC ALGORITHM BACKGROUND

Dominance relationships among different solutions form the basis of Pareto optimization. For a minimization problem involving  $n$  objectives defined by objective functions  $f_n$ , solution  $a$  dominates

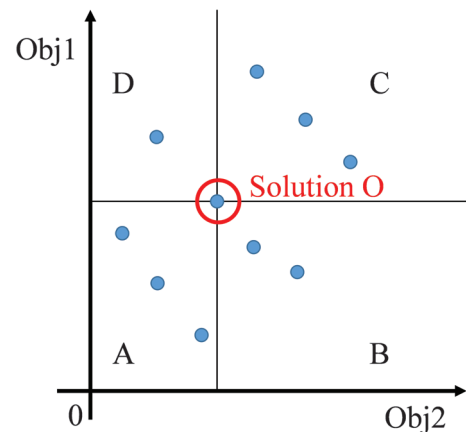


Figure A-1. Dominance concept demonstrated using solution O.

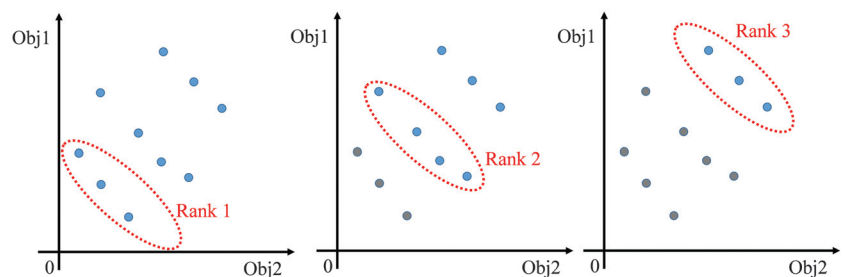


Figure A-2. Solution ranking demonstration.

over solution  $b$  if all objective functions evaluated at solution  $a$  are not greater than those of  $b$ , and at least one objective function of  $a$  is strictly smaller than the corresponding objective function evaluated at solution  $b$  (Park et al., 2015).

The dominance concept can be graphically demonstrated in Figure A-1. For a two-objective optimization problem, we have solution  $O$  shown in the red circle. We draw vertical and horizontal lines crossing solution  $O$  to divide the entire solution space into four regions. In region A,  $obj1$  and  $obj2$  of all three solutions are smaller than those of solution  $O$ . Thus, solutions in region A are better solutions and dominate solution  $O$ . The  $obj1$  and  $obj2$  of solutions in region C are larger than those of solution  $O$ , so solutions in region C are dominated by solution  $O$ . In regions B and D, solutions have one objective smaller but the other objective larger than that of solution  $O$ . Thus, there is no dominance relationship between region B and D solutions and solution  $O$ .

A similar exercise can be performed on every solution to obtain the overall ranking of the solution. In Figure A-2, a set of solutions that are not dominated by any other solutions are classified as rank 1 solutions. When rank 1 solutions are excluded from the solution space, the same exercise is performed in the new solution space to obtain rank 2 solutions. Then, rank 1 and rank 2 solutions are excluded to obtain the next rank level of nondominated solutions. The process is continued until all solutions are assigned a rank level (Park et al., 2015).

The solution ranking exhibits the following features: (1) Solutions on the same rank or same Pareto front are equally optimal, (2) the lower-rank solutions are more competitive than the higher rank ones for a minimization problem, and (3) trade-offs of the front reveal potential conflicts between objectives.

GA is one of the evolutionary methods for solving optimization problems (Goldberg, 1989). It imitates biological principles of evolution — natural selection and survival of the fittest. It has been extensively applied to history-matching problems (Bittencourt and Horne, 1997; Romero and Carter, 2001; Yin et al., 2011; Iino et al., 2017; Park et al., 2019).

In GA, a population of candidate solutions to an optimization problem evolves toward better solutions. Each candidate solution has a set of properties that can be mutated and altered. At the initialization step, the population is generated randomly, providing the range of possible solutions (the search space). During each successive generation, a portion of the existing population is selected to breed a new generation. Individual solutions are selected through a fitness-based process, where fitter solutions (as measured by a fitness function) are more likely to be selected. Certain selection methods rate the fitness of each solution and preferentially select the best solutions. The next step is to generate a second-generation population of solutions from those selected through a combination of genetic operators: crossover (also called recombination) and mutation. For each new solution to be produced, a pair of “parent” solutions is selected for breeding from the pool selected previously. By producing a “child” solution using the above methods of crossover and mutation, a new solution is created, which typically shares many of the characteristics of its “parents.” New parents are selected for each new child, and the process continues until a new population of solutions of appropriate size is generated. These processes ultimately result in the next generation population that is different from the initial generation. Generally, the average fitness will have increased by this procedure for the population because only the best organisms from the first gen-

eration are selected for breeding, along with a small proportion of less-fit solutions. These less-fit solutions ensure genetic diversity within the genetic pool of the parents and therefore ensure the genetic diversity of the subsequent generation of children.

## APPENDIX B

### TUBING HEAD PRESSURE TO BOTTOM HOLE PRESSURE

The tubing head pressure to BHP calculation is routine in the petroleum engineering literature (Govier and Aziz, 1972; Beggs and Brill, 1973; Chen, 1979; Taitel et al., 1982; Bradley, 1987; Ansari et al., 1990; Economides et al., 2013). The calculation below follows Economides et al. (2013). Because both Azle injection wells are wastewater disposal wells, a single-phase incompressible flow model will be used. The Reynolds number needs to be calculated to determine if the flow is laminar or turbulent:

$$N_{re} = \frac{Du\rho}{\mu}, \quad (\text{B-1})$$

where  $D$  is the wellbore diameter,  $u$  is the average velocity,  $\rho$  is the fluid density, and  $\mu$  is the fluid viscosity. If  $N_{re}$  is larger than 2100 (Economides et al., 2013), it is turbulent flow. Otherwise, it is laminar flow.

The overall pressure drop between the well head and the bottom hole consists of three parts: potential energy, kinetic energy, and frictional pressure drop:

$$\Delta p = \Delta p_{PE} + \Delta p_{KE} + \Delta p_F. \quad (\text{B-2})$$

Because there is no change in the inner diameter of the disposal well and thus no change in the velocity of the fluid,  $\Delta p_{KE} = 0$ . The term  $\Delta p_{PE}$  accounts for the pressure change due to the weight of the column of fluid. Because the injected fluid is water, the potential energy change is low and it can be calculated as

$$\Delta p_{PE} = \frac{g}{g_c} \rho \Delta Z, \quad (\text{B-3})$$

where  $\Delta Z$  is the difference in elevation. The frictional pressure drop  $\Delta p_F$  can be obtained from the Fanning equation (Fanning, 1896):

$$\Delta p_F = \frac{2f_f \rho u^2 L}{g_c D}, \quad (\text{B-4})$$

where  $u$  is the velocity and  $f_f$  is the Fanning friction factor:

$$f_f = \begin{cases} \frac{16}{N_{re}}, & N_{re} < 2100 \\ \frac{1}{-4 \log \left( \frac{e}{3.7065} + \frac{5.0452}{N_{re}} \log \left( \frac{e^{1.1098}}{2.8257} + \left( \frac{7.149}{N_{re}} \right)^{0.8981} \right) \right)^2}, & N_{re} > 2100. \end{cases} \quad (\text{B-5})$$

## APPENDIX C

## GAS PRODUCTION CALCULATION

In this study, we convert gas production at the surface condition to the reservoir condition, a routine calculation in reservoir engineering (Dake, 1983; McCain, 1990; Lee and Wattenbarger, 1996; Economides et al., 2013; Ahmed, 2018). The surface gas rate for 70 wells can be obtained from the Railroad Commission of Texas (2018b). The total cumulative production in the surface and reservoir conditions is shown in Figure C-1. A sample calculation for reservoir gas withdrawal rates is provided below.

The gas formation volume factor,  $B_g$ , defined as the ratio of the volume of gas at the reservoir temperature and pressure to the volume at the standard temperature and pressure, can be calculated by rearranging the real gas equation (Dake, 1983):

$$B_g = \frac{V_{res}}{V_{sc}} = \frac{p_{sc} z T}{Z_{sc} T_{sc} p_{res}}. \quad (C-1)$$

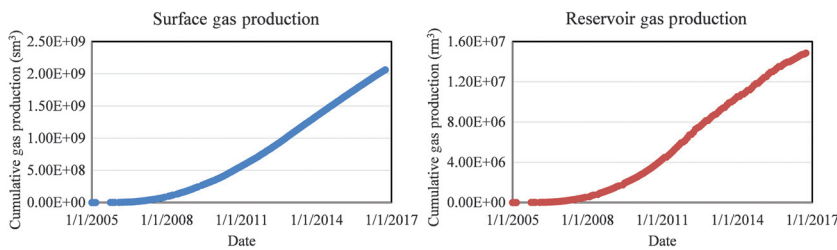


Figure C-1. Cumulative gas production for 70 wells at surface and reservoir conditions.

Table C-1. Gas composition and critical pressure and temperature calculation.

	C <sub>1</sub>	C <sub>2</sub>	C <sub>3</sub>	CO <sub>2</sub>	N <sub>2</sub>	Mixture
Gas composition	93.7	2.6	0	2.7	1	—
Critical temperature (°R)	343.30	549.90	666.10	547.80	227.40	—
Critical pressure (psi)	666.00	708.00	616.00	1071.60	493.10	—
$y_i T_c$	321.67	14.30	0	14.79	2.27	353.0
$y_i P_c$	624.04	18.41	0	28.93	4.93	676.3

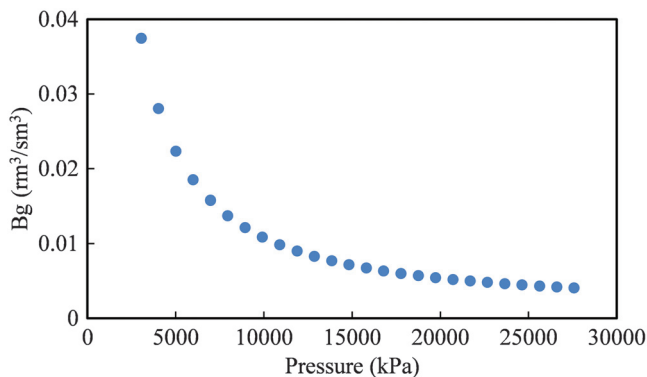


Figure C-2. Gas formation volume factor generated from commercial PVT simulator.

The standard condition pressure and temperature are

$$p_{sc} = 101 \text{ kPa} (14.7 \text{ psi}). \quad (C-2)$$

$$T_{sc} = 15.7^\circ\text{C} (520^\circ\text{R}). \quad (C-3)$$

We use a pressure gradient of 10.2 kPa/m (0.45 psi/ft) and a geothermal gradient of 0.0219°C/m (12°F/1000 ft) (Syms, 2011). The average depth for Barnett is 2100 m (6888 ft). We can then calculate reservoir pressure and temperature:

$$p_{res} = 21,374 \text{ kPa} (3100 \text{ psi}). \quad (C-4)$$

$$T_{res} = 62^\circ\text{C} (603^\circ\text{R}). \quad (C-5)$$

The only unknown is the gas compressibility factor  $Z$ , which requires the gas composition. The gas composition is shown in Table C-1 (Hill et al., 2007).

Knowing the gas compressibility, we estimate the  $Z$ -factor to be 0.82 (McCain, 1990). Substituting back into equation C-1, we obtain

$$B_g = 0.00451 \frac{\text{rm}^3}{\text{sm}^3}, \quad (C-6)$$

where  $\text{rm}^3$  is the cubic meter in reservoir conditions and  $\text{sm}^3$  is the cubic meter in standard conditions.

In our simulation,  $B_g$  is a dynamic parameter based on the calculated BHP and Figure C-2.

## REFERENCES

- Ahmed, T., 2018, Reservoir engineering handbook: Gulf Professional Publishing.
- Aki, K., and P. G. Richards, 2002, Quantitative seismology: University Science Books.
- Ansari, A. M., N. D. Sylvester, O. Shoham, and J. P. Brill, 1990, A comprehensive mechanistic model for upward two-phase flow in wellbores: Annual Technical Conference and Exhibition, SPE 20630.
- Beggs, D. H., and J. P. Brill, 1973, A study of two-phase flow in inclined pipes: Journal of Petroleum Technology, **25**, 607–617, doi: 10.2118/4007-PA.
- Bittencourt, A. C., and R. N. Horne, 1997, Reservoir development and design optimization: Annual Technical Conference and Exhibition, SPE 38895.
- Bourouis, S., and P. Bernard, 2007, Evidence for coupled seismic and aseismic fault slip during water injection in the geothermal site of Soultz (France), and implications for seismic transients: Geophysical Journal International, **169**, 723–732, doi: 10.1111/j.1365-246X.2006.03325.x.
- Bradley, H. B., 1987, Petroleum engineering handbook: SPE.
- Breiman, L., J. Friedman, C. J. Stone, and R. A. Olshen, 1984, Classification and regression trees: Taylor & Francis.
- Castiñeira, D., B. Jha, and R. Juanes, 2016, Uncertainty quantification and inverse modeling of fault poromechanics and induced seismicity: Application to a synthetic carbon capture and storage (CCS) problem: 50th US Rock Mechanics/Geomechanics Symposium, ARMA 2016-151.
- Chang, K. W., and P. Segall, 2016a, Injection-induced seismicity on basement faults including poroelastic stressing: Journal of Geophysical Research: Solid Earth, **121**, 2708–2726, doi: 10.1002/2015JB012561.
- Chang, K. W., and P. Segall, 2016b, Seismicity on basement faults induced by simultaneous fluid injection-extraction: Pure and Applied Geophysics, **173**, 2621–2636, doi: 10.1007/s00024-016-1319-7.
- Chang, K. W., and H. Yoon, 2018, 3-D modeling of induced seismicity along multiple faults: Magnitude, rate, and location in a poroelasticity system:

- Journal of Geophysical Research: Solid Earth, **123**, 9866–9883, doi: [10.1029/2018JB016446](https://doi.org/10.1029/2018JB016446).
- Chen, N. H., 1979, An explicit equation for friction factor in pipe: *Industrial & Engineering Chemistry Fundamentals*, **18**, 296–297, doi: [10.1021/i160071a019](https://doi.org/10.1021/i160071a019).
- Computer Modeling Group, 2016, STARS user guide (version 2016.10): Computer Modeling Group Ltd.
- Dahm, T., and F. Krüger, 2014, Moment tensor inversion and moment tensor interpretation, P. Bormann, ed., *New manual of seismological observatory practice*: Deutsches Geoforschungszentrum GFZ, 1–37, doi: [10.2312/GFZ.NMSOP-2\\_IS\\_3.9](https://doi.org/10.2312/GFZ.NMSOP-2_IS_3.9).
- Dake, L. P., 1983, *Fundamentals of reservoir engineering*: Elsevier.
- DeShon, H. R., C. T. Hayward, P. O. Ogwari, L. Quinones, O. Sufri, B. Stump, and M. Beatrice Magnani, 2018, Summary of the North Texas earthquake study seismic networks, 2013–2018: *Seismological Research Letters*, **90**, 387–394, doi: [10.1785/0220180269](https://doi.org/10.1785/0220180269).
- Drillinginfo, 2018, Online research queries, <https://info.drillinginfo.com/>, accessed 1 May 2017.
- Economides, M. J., A. D. Hill, C. Ehlig-Economides, and D. Zhu, 2013, *Petroleum production systems*: Pearson Education.
- Ellsworth, W. L., 2013, Injection-induced earthquakes: *Science*, **341**, 1225942, doi: [10.1126/science.1225942](https://doi.org/10.1126/science.1225942).
- Ewing, T. E., 1991, *The tectonic framework of Texas*: Bureau of Economic Geology, University of Texas.
- Fan, Z., P. Eichhubl, and J. F. W. Gale, 2016, Geomechanical analysis of fluid injection and seismic fault slip for the Mw4. 8 Timpson, Texas, earthquake sequence: *Journal of Geophysical Research: Solid Earth*, **121**, 2798–2812, doi: [10.1002/2016JB012821](https://doi.org/10.1002/2016JB012821).
- Fanning, J. T., 1896, *A practical treatise on hydraulic and water-supply engineering*: D. Van Nostrand Company.
- Frohlich, C., H. DeShon, B. Stump, C. Hayward, M. Hornbach, and J. I. Walter, 2016, A historical review of induced earthquakes in Texas: *Seismological Research Letters*, **87**, 1022–1038, doi: [10.1785/0220160016](https://doi.org/10.1785/0220160016).
- Frohlich, C., C. Hayward, B. Stump, and E. Potter, 2011, The Dallas–Fort Worth earthquake sequence: October 2008 through May 2009: *Bulletin of the Seismological Society of America*, **101**, 327–340, doi: [10.1785/0120100131](https://doi.org/10.1785/0120100131).
- Goldberg, D. E., 1989, *Genetic algorithms in search, optimization and machine learning*: Addison-Wesley Longman Publishing Company.
- Gono, V., J. E. Olson, and J. F. Gale, 2015, Understanding the correlation between induced seismicity and wastewater injection in the Fort Worth Basin: 49th U.S. Rock Mechanics/Geomechanics Symposium, ARMA 2015-419.
- Govier, G. W., and K. Aziz, 1972, *The flow of complex mixtures in pipes*: Van Nostrand Reinhold Company.
- Guglielmi, Y., F. Cappa, J.-P. Avouac, P. Henry, and D. Elsworth, 2015, Seismicity triggered by fluid injection-induced aseismic slip: *Science*, **348**, 1224–1226, doi: [10.1126/science.aab0476](https://doi.org/10.1126/science.aab0476).
- Hennings, P., A. Savvaiddis, M. Young, E. Rathje, M. Babazadeh, T. Borgfeldt, R. Chen, A. Datta-Gupta, H. DeShon, P. Eichhubl, Z. Fan, C. Frohlich, V. Gono, J. Kim, M. King, C. Lemons, T. Mukherjee, J.-P. Nicot, J. Olson, J. Park, J. Walter, X. Xue, H. Yoon, B. Young, and G. Zalachoris, 2016, Report on house bill 2 (2016-17) seismic monitoring and research in Texas, <http://www.beg.utexas.edu/files/textnet-cisr/Report%20Assets/TextNet-Report-2016.pdf>, accessed 2 September 2019.
- Hill, R. J., D. M. Jarvie, J. Zumberge, M. Henry, and R. M. Pollastro, 2007, Oil and gas geochemistry and petroleum systems of the Fort Worth Basin: *AAPG Bulletin*, **91**, 445–473, doi: [10.1306/11030606014](https://doi.org/10.1306/11030606014).
- Hornbach, M. J., H. R. DeShon, W. L. Ellsworth, B. W. Stump, C. Hayward, C. Frohlich, H. R. Oldham, J. E. Olson, M. B. Magnani, and C. Brokaw, 2015, Causal factors for seismicity near Azle, Texas: *Nature Communications*, **6**, 6728, doi: [10.1038/ncomms7728](https://doi.org/10.1038/ncomms7728).
- Hornbach, M. J., M. Jones, M. Scales, H. R. DeShon, M. B. Magnani, C. Frohlich, B. Stump, C. Hayward, and M. Layton, 2016, Ellenburger wastewater injection and seismicity in North Texas: *Physics of the Earth and Planetary Interiors*, **261**, 54–68, doi: [10.1016/j.pepi.2016.06.012](https://doi.org/10.1016/j.pepi.2016.06.012).
- Iino, A., A. Vyas, J. Huang, A. Datta-Gupta, Y. Fujita, N. Bansal, and S. Sankaran, 2017, Efficient modeling and history matching of shale oil reservoirs using the fast marching method: Field application and validation: Western Regional Meeting, SPE 185719.
- Kanamori, H., 1977, The energy release in great earthquakes: *Journal of Geophysical Research*, **82**, 2981–2987, doi: [10.1029/JB082i020p02981](https://doi.org/10.1029/JB082i020p02981).
- Lee, W. J., and R. A. Wattenbarger, 1996, *Gas reservoir engineering*: SPE.
- Lele, S. P., S. Y. Hsu, J. L. Garzon, N. DeDontney, K. H. Searles, G. A. Gist, P. F. Sanz, E. A. Biediger, and B. A. Dale, 2016, Geomechanical modeling to evaluate production-induced seismicity at Groningen field: Abu Dhabi International Petroleum Exhibition & Conference, SPE 183554.
- Loucks, R. G., R. M. Reed, S. C. Ruppel, and D. M. Jarvie, 2009, Morphology, genesis, and distribution of nanometer-scale pores in siliceous mudstones of the Mississippi Barnett Shale: *Journal of Sedimentary Research*, **79**, 848–861, doi: [10.2110/jsr.2009.092](https://doi.org/10.2110/jsr.2009.092).
- Lund Snee, J., and M. D. Zoback, 2016, State of stress in Texas: Implications for induced seismicity: *Geophysical Research Letters*, **43**, 10,208–10,214, doi: [10.1002/2016GL070974](https://doi.org/10.1002/2016GL070974).
- McCain, W. D., 1990, *The properties of petroleum fluids*: PennWell Books.
- McGarr, A., and A. J. Barbour, 2017, Wastewater disposal and the earthquake sequences during 2016 near Fairview, Pawnee, and Cushing, Oklahoma: *Geophysical Research Letters*, **44**, 9330–9336, doi: [10.1002/2017GL075258](https://doi.org/10.1002/2017GL075258).
- McGarr, A., D. Simpson, L. Seeber, and W. Lee, 2002, Case histories of induced and triggered seismicity: *International Geophysics Series*, **81**, 647–661, doi: [10.1016/S0074-6142\(02\)80243-1](https://doi.org/10.1016/S0074-6142(02)80243-1).
- Mishra, S., and A. Datta-Gupta, 2017, *Applied statistical modeling and data analytics: A practical guide for the petroleum geosciences*: Elsevier.
- National Research Council, 2013, *Induced seismicity potential in energy technologies*: National Academies Press.
- Park, H. Y., A. Datta-Gupta, and M. J. King, 2015, Handling conflicting multiple objectives using Pareto-based evolutionary algorithm during history matching of reservoir performance: *Journal of Petroleum Science and Engineering*, **125**, 48–66, doi: [10.1016/j.petrol.2014.11.006](https://doi.org/10.1016/j.petrol.2014.11.006).
- Park, J., A. Iino, A. Datta-Gupta, J. Bi, and S. Sankaran, 2019, Rapid modeling of injection and production phases of hydraulically fractured shale wells using the fast marching method: Unconventional Resources Technology Conference, SPE/AAPG/SEG, URTEC 2019–339.
- Park, J., J. Kim, and D. Zhu, 2016, Assessment of potential fault activation in Tarim Basin during hydraulic fracturing operations by using rigorous simulation of coupled flow and geomechanics: Asia Pacific Hydraulic Fracturing Conference, SPE 181811.
- Pollastro, R. M., D. M. Jarvie, R. J. Hill, and C. W. Adams, 2007, Geologic framework of the Mississippi Barnett Shale, Barnett-Paleozoic total petroleum system, bend arch-Fort Worth Basin, Texas: *AAPG Bulletin*, **91**, 405–436, doi: [10.1306/103006060008](https://doi.org/10.1306/103006060008).
- Quinones, L. A., H. R. DeShon, M. B. Magnani, and C. Frohlich, 2018, Stress orientations in the Fort Worth Basin, Texas, determined from earthquake focal mechanisms: *Bulletin of the Seismological Society of America*, **108**, 1124–1132, doi: [10.1785/0120170337](https://doi.org/10.1785/0120170337).
- Railroad Commission of Texas, 2015a, Proposal for decision, oil and gas docket no. 09-0296410, <https://www.rrc.state.tx.us/media/31022/09-96410-sho-pfd.pdf>, accessed 2 September 2019.
- Railroad Commission of Texas, 2015b, Proposal for decision, oil and gas docket no. 09-0296411, <https://www.rrc.state.tx.us/media/31023/09-96411-sho-pfd.pdf>, accessed 2 September 2019.
- Railroad Commission of Texas, 2018a, H10 filing system, <http://webapps.rrc.state.tx.us/H10/h10PublicMain.do>, accessed 1 May 2018.
- Railroad Commission of Texas, 2018b, Online research queries, <https://www.rrc.texas.gov/about-us/resource-center/research/online-research-queries/>, accessed 7 November 2018.
- Reasenber, P. A., and R. W. Simpson, 1992, Response of regional seismicity to the static stress change produced by the Loma Prieta earthquake: *Science*, **255**, 1687–1690, doi: [10.1126/science.255.5052.1687](https://doi.org/10.1126/science.255.5052.1687).
- Romero, C. E., and J. N. Carter, 2001, Using genetic algorithms for reservoir characterization: *Journal of Petroleum Science and Engineering*, **31**, 113–123, doi: [10.1016/S0920-4105\(01\)00124-3](https://doi.org/10.1016/S0920-4105(01)00124-3).
- Rutqvist, J., A. P. Rinaldi, F. Cappa, and G. J. Mordis, 2013, Modeling of fault reactivation and induced seismicity during hydraulic fracturing of shale-gas reservoirs: *Journal of Petroleum Science and Engineering*, **107**, 31–44, doi: [10.1016/j.petrol.2013.04.023](https://doi.org/10.1016/j.petrol.2013.04.023).
- Sanz, P. F., S. P. Lele, K. H. Searles, S. Y. Hsu, J. L. Garzon, J. A. Burdette, W. E. Kline, B. A. Dale, and P. D. Hector, 2015, Geomechanical analysis to evaluate production-induced fault reactivation at Groningen gas field: Annual Technical Conference and Exhibition, SPE 174942.
- Schwab, D. R., T. S. Bidgoli, and M. H. Taylor, 2017, Characterizing the potential for injection-induced fault reactivation through subsurface structural mapping and stress field analysis, Wellington Field, Sumner County, Kansas: *Journal of Geophysical Research: Solid Earth*, **122**, 132–154, doi: [10.1002/2017JB014071](https://doi.org/10.1002/2017JB014071).
- Segall, P., 1989, Earthquakes triggered by fluid extraction: *Geology*, **17**, 942–946, doi: [10.1130/0091-7613\(1989\)017<0942:ETBFE>2.3.CO;2](https://doi.org/10.1130/0091-7613(1989)017<0942:ETBFE>2.3.CO;2).
- Segall, P., J. R. Grasso, and A. Mossop, 1994, Poroelastic stressing and induced seismicity near the Lacq gas field, southwestern France: *Journal of Geophysical Research: Solid Earth*, **99**, 15423–15438, doi: [10.1029/94JB00989](https://doi.org/10.1029/94JB00989).
- Segall, P., and S. Lu, 2015, Injection-induced seismicity: Poroelastic and earthquake nucleation effects: *Journal of Geophysical Research: Solid Earth*, **120**, 5082–5103, doi: [10.1002/2015JB012060](https://doi.org/10.1002/2015JB012060).
- Simpson, R. W., 1997, Quantifying Anderson’s fault types: *Journal of Geophysical Research: Solid Earth*, **102**, 17909–17919, doi: [10.1029/97JB01274](https://doi.org/10.1029/97JB01274).
- Sone, H., and M. D. Zoback, 2013, Mechanical properties of shale-gas reservoir rocks — Part 1: Static and dynamic elastic properties and anisotropy: *Geophysics*, **78**, no. 5, D381–D392, doi: [10.1190/geo2013-0050.1](https://doi.org/10.1190/geo2013-0050.1).

- Stein, R. S., 1999, The role of stress transfer in earthquake occurrence: *Nature*, **402**, 605–609, doi: [10.1038/45144](https://doi.org/10.1038/45144).
- Sullivan, E. C., K. J. Marfurt, A. Lacazette, and M. Ammerman, 2006, Application of new seismic attributes to collapse chimneys in the Fort Worth Basin: *Geophysics*, **71**, no. 4, B111–B119, doi: [10.1190/1.2216189](https://doi.org/10.1190/1.2216189).
- Syms, F., 2011, Technical issues related to hydraulic fracturing and fluid extraction/injection near the Comanche Peak nuclear facility in Texas, <https://www.nrc.gov/docs/ML1131/ML11314A197.pdf>, accessed 2 September 2019.
- Taitel, Y., D. Barnea, and A. Dukler, 1982, A film model for the prediction of flooding and flow reversal for gas-liquid flow in vertical tubes: *International Journal of Multiphase Flow*, **8**, 1–10, doi: [10.1016/0301-9322\(82\)90002-7](https://doi.org/10.1016/0301-9322(82)90002-7).
- Tutuncu, A. N., 2010, Anisotropy, compaction and dispersion characteristics of reservoir and seal shales: 44th U.S. Rock Mechanics Symposium and 5th U.S.-Canada Rock Mechanics Symposium, ARMA, 10-344.
- Vermeer, P. A., and R. De Borst, 1984, Non-associated plasticity for soils, concrete and rock: *Heron*, **29**, 1–64.
- Wang, H., 2000, *Theory of linear poroelasticity with applications to geomechanics and hydrogeology*: Princeton University Press.
- Yin, J., H. Y. Park, A. Datta-Gupta, M. J. King, and M. K. Choudhary, 2011, A hierarchical streamline-assisted history matching approach with global and local parameter updates: *Journal of Petroleum Science and Engineering*, **80**, 116–130, doi: [10.1016/j.petrol.2011.10.014](https://doi.org/10.1016/j.petrol.2011.10.014).
- Zhai, G., and M. Shirzaei, 2018, Fluid injection and time-dependent seismic hazard in the Barnett Shale, Texas: *Geophysical Research Letters*, **45**, 4743–4753, doi: [10.1029/2018GL077696](https://doi.org/10.1029/2018GL077696).
- Zhang, Y., M. Person, J. Rupp, K. Ellett, M. A. Celia, C. W. Gable, B. Bowen, J. Evans, K. Bandilla, P. Mozley, T. Dewers, and T. Elliot, 2013, Hydrogeologic controls on induced seismicity in crystalline basement rocks due to fluid injection into basal reservoirs: *Groundwater*, **51**, 525–538, doi: [10.1111/gwat.12071](https://doi.org/10.1111/gwat.12071).
- Zoback, M. D., A. Kohli, I. Das, and M. W. McClure, 2012, The importance of slow slip on faults during hydraulic fracturing stimulation of shale gas reservoirs: Americas Unconventional Resources Conference, SPE 155476.